Article Type: Research Article

Europium-155 as a source for dual energy cone beam computed tomography in adaptive proton therapy: a simulation study

Jiahua Zhu[1], Scott N. Penfold[1,2]

[1]Department of Physics, University of Adelaide, Adelaide, SA 5005, Australia
[2]Department of Medical Physics, Royal Adelaide Hospital, Adelaide, SA 5000, Australia

Contact details of the corresponding author:

scott.penfold@sa.gov.au

The authors have no conflict of interest or financial disclosures to report.

Abstract

Purpose: To investigate the feasibility of a 3D imaging system utilizing a ^{155}Eu source and pixelated cadmium-zinc-telluride (CZT) detector for applications in adaptive radiotherapy. Specifically, to compare the reconstructed stopping power ratio (SPR) values of a head phantom obtained with the proposed imaging technique with theoretical SPR values.

Method: A Geant4 Monte Carlo simulation was performed with the novel imaging system. The simulation was repeated with a typical 120 kV X-ray tube spectrum while maintaining all other parameters. Dual energy ^{155}Eu source CBCT images were reconstructed with an iterative projection

This article has been accepted for publication and undergone full peer review but has not been through the copyediting, typesetting, pagination and proofreading process, which may lead to differences between this version and the Version of Record. Please cite this article as doi: 10.1002/mp.12450

algorithm known as total variation superiorization with diagonally relaxed orthogonal projections (TVS-DROP). Single energy 120 kV source CBCT images were also reconstructed with TVS-DROP. Reconstructed images were converted to SPR with stoichiometric calibration techniques based on ICRU 44 tissues. Quantitative accuracy of reconstructed attenuation coefficient images as well as SPR images were compared.

Results: Images generated by gamma emissions of ^{155}Eu showed superior contrast resolution to those generated by the 120 kV spectrum. Quantitatively, all reconstructed images correlated with reference attenuation coefficients of the head phantom within 1 standard deviation. Images generated with the ^{155}Eu source showed a smaller standard deviation of pixel values. Use of a dual energy conversion to SPR resulted in superior SPR accuracy with the ^{155}Eu.

Conclusion: ^{155}Eu was found to display desirable qualities when used as a source for dual energy CBCT. Further work is required to demonstrate whether the simulation results presented here can be translated into an experimental prototype.

Keywords

Europium-155, dual energy cone beam computed tomography, adaptive proton therapy, pixelated cadmium-zinc-telluride detectors.

1. Introduction

Proton therapy is a highly conformal form of external beam radiotherapy. To fully exploit the physical advantages of proton therapy, the geometry and stopping power ratio (SPR) of patient tissues at the time of treatment should be known with a high degree of accuracy. Cone beam computed tomography (CBCT) is a popular tool for obtaining three dimensional geometrical information at the time of

treatment in X-ray therapy. In more advanced treatment workflows, CBCT can also be used as a tool for dose accumulation studies and offline adaptive radiotherapy[1,2]. Despite the widespread use of CBCT in conventional X-ray radiotherapy, this technology is only now becoming a standard offering of proton therapy vendors. The most effective utilization of CBCT in a clinical proton therapy environment is a topic receiving increasing interest[3-6].

Due to the dependence of CBCT Hounsfield units (HUs) on the particular scatter environment created by the patient, CBCT image data are not typically used directly for dose calculation[7,8]. Rather, CBCT images are typically only used for geometrical information in online use. In offline adaptive radiotherapy, however, the original planning CT may be registered to the CBCT geometry with rigid or deformable image registration algorithms and dose calculation performed on this data set. This allows for dose accumulation studies and assessment of the need for replanning during the course of treatment. While this is undoubtedly a step in the right direction, a CBCT system capable of producing reliable HUs may allow for efficient *online* adaptive radiotherapy.

Furthermore, a number of recent studies have examined the potential advantages of dual energy CT (DECT) for proton therapy dose calculation[9-11]. Various DECT scanning approaches have been proposed, however the most common scenario consists of imaging with two differing X-ray spectra emanating from an X-ray tube. The resulting reconstructed images can be processed to produce images of electron density and effective atomic number[9-11]. The effective atomic number data can be correlated with mean excitation energy, allowing for a calculation of stopping power[9,11]. This approach has been shown to result in superior dose calculation accuracy for proton therapy in certain cases when compared to the standard approach based on single energy CT and an empirically derived conversion of HU to SPR.

Despite the promising results obtained thus far with DECT for proton therapy, a number of technical and logistical issues need to be addressed. Firstly, beam hardening of the polyenergetic bremsstrahlung

spectra emitted from X-ray tubes means that a given tissue does not possess a unique effective atomic number, as determined from DECT. Rather, the effective atomic number is dependent on the spectral composition at the point of the tissue, which will differ at different projection angles. This results in a lack of data fidelity. Furthermore, truly coincident DECT imaging with X-ray sources differing in energy is not possible. The acquired data is either temporally separated in the case of kV switching of a single tube, or sequential scanning at different tube potentials, or spatially separated in the case dual tubes operating at different angles simultaneously. Promising advances have been made in detector based DECT, however, as seen by the release of the Philips (Koninklijke Philips N.V. 2004-2014) IQon Spectral CT. This device makes use of two photon detector layers of different energy response to separate "low" and "high" energy photons. Beam hardening is still present in this approach, however.

In the current work a dual energy CBCT (DECBCT) system making use of Europium-155 (^{155}Eu) and a pixelated detector capable of energy discrimination is proposed to meet the needs for accurate online dose calculation in proton therapy. A description of the favorable characteristics of ^{155}Eu for this purpose is presented. A Monte Carlo simulation of a CBCT acquisition of a head phantom with ^{155}Eu and a pixelated cadmium-zinc-telluride (CZT) detector was conducted. The resulting reconstruction of SPR was compared to a corresponding simulation with a 120 kV bremsstrahlung spectrum simulating a conventional CBCT system.

2. Methods

2.1. Characteristics of ^{155}Eu

^{155}Eu was first investigated as a potential source for mobile X-ray imaging by Stewart[12] in the 1950s. The primary properties that make ^{155}Eu an attractive source for dual energy imaging are; a half-life that is not excessively long so as to be a serious radiation waste concern, while long enough to ensure reasonable periods between source replacement; two dominant gamma emissions between 50 and 150

keV to eliminate beam hardening; a high specific activity allowing for a high activity in a small volume; and an observationally stable daughter isotope. These characteristics are summarized in Table 1 with γ emissions summarized in Table 2.

^{155}Eu can be produced through neutron irradiation of enriched ^{154}Sm. The (n,γ) reaction channel produces ^{155}Sm which subsequently decays through β^- decay with a 22 minute half-life[13]. A drawback of this reaction channel is the simultaneous production of ^{154}Eu through the (n,γ) reaction of ^{153}Eu which may be produced by neutron irradiation of contaminant ^{152}Sm. The ratio of ^{154}Eu:^{155}Eu can be minimized by high purity ^{154}Sm, a short irradiation time and frequent target reprocessing to remove stable ^{153}Eu. Case *et al.*[13] suggest that enriched ^{154}Sm containing 98.5% ^{154}Sm and 1.25% ^{152}Sm irradiated at 2×10^{14} neutrons/cm^2/s for 2 days should yield 0.17 Ci of ^{155}Eu per gram of samarium. The ratio of ^{154}Eu: ^{155}Eu would be $3 - 8 \times 10^{-4}$ Ci/Ci.

Table 1. Characteristics of ^{155}Eu[14].

Characteristic	Value
Half-life	4.753 yr
Decay mode	β^- (100%)
Q-value	252.1 keV
Molar mass	154.92 g/mol
Specific activity	1.79×10^{13} Bq/g
Daughter nucleus	^{155}Gd

Table 2. γ energies of ^{155}Eu [14]. Probabilities correspond to gammas per decay. Energies utilized in the proposed imaging are shown in bold.

Energy (keV)	Probability (%)
12.7	0.01
13.8	0.02
18.8	0.05
24.6	0.01
26.5	0.32
31.4	0.01
40.8	0.03
45.3	1.33
58.0	0.07
60.0	1.13
86.1	0.15
86.5	**30.70**
105.3	**21.15**
146.1	0.05

When imaging with a radioactive source, one must consider the volume of the source required to acquire images in a realistic timeframe. The following calculation was performed to determine an approximate source size required for image acquisition with dual energies at 86.5 keV and 105.3 keV. If too large a source size is required, spatial resolution may be compromised.

Firstly, the counts of each gamma energy per pixel required to maintain a σ = 2% uncertainty due to Poisson counting statistics was calculated with Eq. (1).

$$N = \sigma^{-2} \quad (1)$$

The detector was assumed to be 500 mm from imaging isocentre (ADD) with a pixel size of 1 mm (d) and a total area of 500 × 500 mm^2 (side length of l = 500 mm). If the source is 1000 mm from isocentre (SAD), this pixel size equates to 0.67 mm at the isocentre plane, with a 333 mm field of view. The fractional area (a) of a single pixel at the edge of the detector in the 4π geometry surrounding the source was approximated with Eq. (2).

$$a = \frac{d^2}{4\pi((SAD+ADD)^2+(l/2)^2)} \quad (2)$$

A rotation speed of 1 revolution per minute was assumed with angular binning of 2 degrees. This equates to an acquisition time of t_p = 0.33 s per projection. The activity *A* required to deliver *N* counts of each gamma energy per pixel per projection angle after traversing a 200 mm thick water phantom was calculated with Eq. (3).

$$A = \frac{N}{exp(-\mu_w(E)D)} \frac{f(E)}{a} \frac{1}{t_p} \quad (3)$$

Where, μ_w is the attenuation coefficient of water at gamma energy *E*, *D* is the thickness of a water phantom, here estimated to be 200 mm, and *f*(*E*) is the fraction of gammas of energy *E* emitted per decay of ^{155}Eu. The specific activity of a pure sample of ^{155}Eu was calculated with Eq. (4)

$$s = \frac{N_A \ln 2}{t_{1/2} M_A} \quad (4)$$

Using Eq.'s (3) and (4), the mass of ^{155}Eu required is

$$m = A/s \quad (5)$$

Using the values defined in the text and Table 1, a spherical source of diameter 4.0 mm and 4.2 mm were required for the 86. 5 keV and 105.3 keV gammas respectively. In the following Geant4 Monte Carlo simulations, a conservative spherical source of 5.0 mm diameter was used. Assuming 100% ^{155}Eu purity, this corresponds to an activity of 6.15 × 10^{12} Bq.

2.2. Monte Carlo simulation

The Geant4 Monte Carlo toolkit[15] was used to model the DECBCT system with the geometry and materials outlined above. All simulations were performed with Geant4 version 10.0.0.p03 with the EmStandard_Opt4 electromagnetic physics processes enabled. This physics constructor makes use of the Evaluated Photon Data Library 1997[16].

2.2.1. Source spectra

To include the effects of source self-attenuation, a preliminary simulation with a 5.0 mm diameter source of ^{155}Eu material surrounded by an air sensitive detector shell was conducted. The Geant4 General Particle Source (GPS) was used with ^{155}Eu ions of zero kinetic energy to generate primary events. These primaries decayed with the Geant4 Radioactive Decay version 4.0 dataset. All emissions exiting the ^{155}Eu source were collected by the sensitive detector. A plot of collected emissions with and without source attenuation are shown in Fig. 1. The collected photon emissions with source attenuation were used as a phase-space file for further imaging simulations. Electrons were not included in imaging simulations as they significantly slow processing and would be attenuated in air before reaching the imaged object.

The source for subsequent simulations was modelled as a 5.0 mm diameter sphere of air. A histogram of 1 keV bin width containing the photon energy distribution collected in the ^{155}Eu source simulation was used with Geant4 GPS. All primary particles were now photons. The primary photons were restricted to a conical initial direction covering the detector panel. To shape the conical emission to the panel area, a lead collimator was placed in the Geant4 geometry to form a pyramid shaped primary beam, matching the detector area.

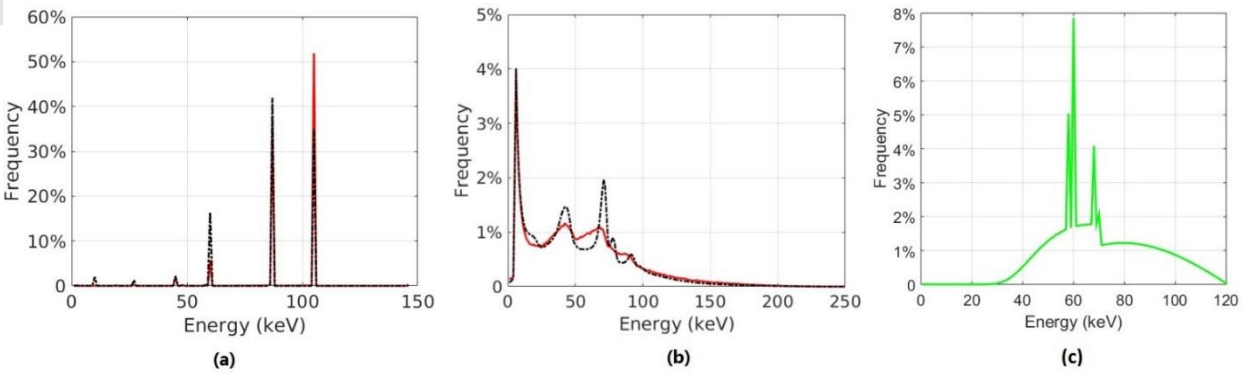

Figure 1. ^{155}Eu spectra generated by Geant4 with (red) and without (black) source self-attenuation. (a) Photon energy spectrum, (b) electron energy spectrum. (c) 120 kV bremsstrahlung spectrum used for polyenergetic X-ray tube comparison.

2.2.2. Phantom

A head phantom with a geometry suggested by Herman[17] was placed at the centre of rotation of the imaging system. The phantom simulated a human head structure with skull, brain and four types of soft tissue materials. The chemical compositions and densities of the tissues are shown in Table 3. A cross-section of the phantom is shown in Fig. 2(a). The outer dimensions of the head phantom were 17.3 cm × 12.9 cm. The Geant4 simulation geometry is shown in Fig. 2(b).

Table 3. Elemental fractions by weight and density of 6 tissues included in the head phantom.

Tissue	H	C	N	O	P	Na	S	Cl	K	Density (g/cm^3)
Cranium[18]	0.005	0.212	0.040	0.435	0.002	0.081	0.003	0.176	0.001	1.610
Brain[18]	0.107	0.145	0.022	0.712	0.004	0.002	0.002	0.003	0.003	1.035
Cerebrospinal fluid (CSF)	0.112	0	0	0.888	0	0	0	0	0	0.900
Haematoma	0.107	0.145	0.022	0.712	0.004	0.002	0.002	0.003	0.003	1.050
Carcinoma	0.107	0.145	0.022	0.712	0.004	0.002	0.002	0.003	0.003	1.200
Meningoma	0.107	0.145	0.022	0.712	0.004	0.002	0.002	0.003	0.003	1.150

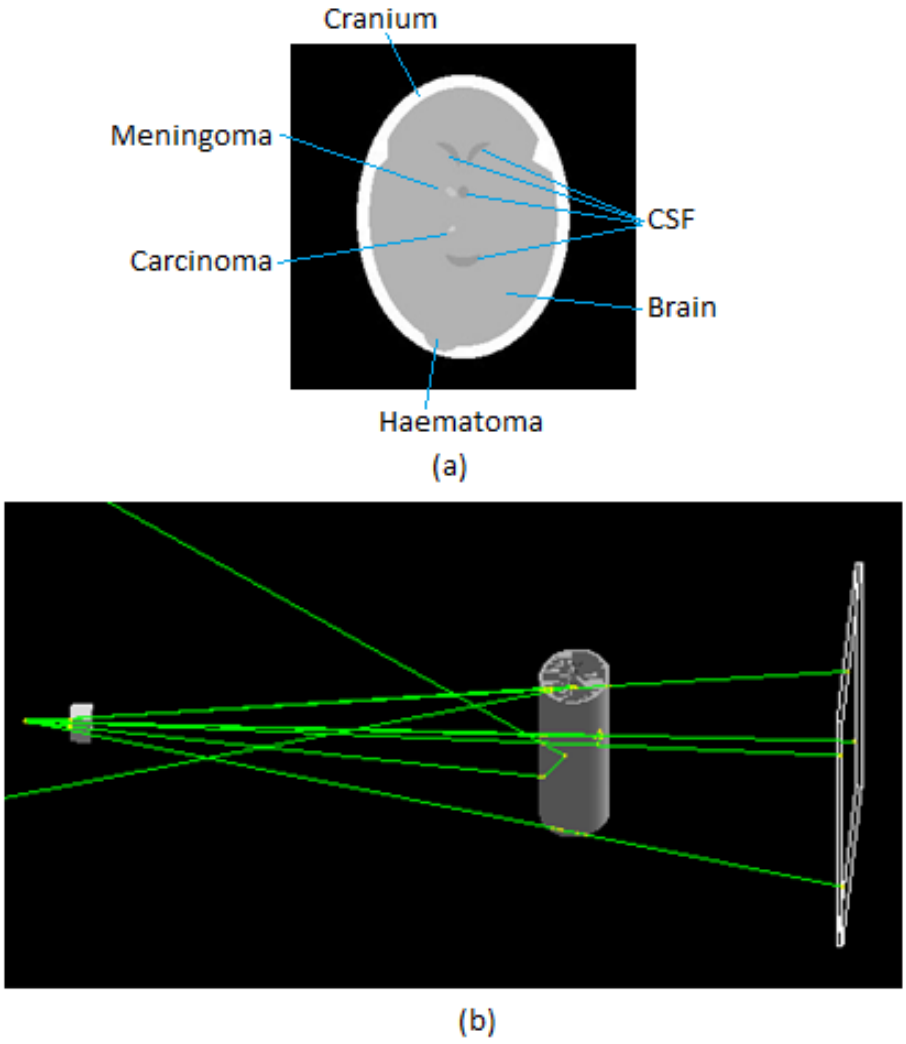

Figure 2. (a) Cross-section of the head phantom used in the imaging simulations. The white region represents cranial bone, the main inner region represents brain tissue. All dark grey regions are CSF, the upper small ellipse is a meningioma and the lower small ellipse is a carcinoma. (b) Simulation geometry in Geant4. Primary photons are emitted from the source volume on the left, pass through a lead collimator, interact or traverse the cylindrical phantom, and are incident on the pixelated detector panel.

2.2.3. Pixelated detector

Current flat panel imaging systems are often composed of a scintillating material bonded to an amorphous silicon (aSi) thin film transistor (TFT) array. The high atomic number scintillating material is used to improve the photon detection efficiency of the device. The readout of these systems is typically not spectroscopic, but rather energy integrating. Pixelated direct detection semiconductors, and cadmium-zinc-telluride (CZT) detectors in particular, are experiencing growing interest from the medical imaging community. The high atomic number and suitability for room temperature operation of these devices make them ideal for spectroscopy in the energy range of the ^{155}Eu emissions. A comparison of imaging efficiency with a conventional flat panel consisting of CsI bonded to aSi and CZT panels has been performed by Le *et al*.[19].

A pixelated CZT detector panel was simulated in the Geant4 imaging simulations. The panel was 10 mm thick with 1 mm pixel sizes and a total area of 500 × 500 mm^2. The panel was positioned 500 mm from the centre of rotation of the imaging system. The panel was simulated as a solid slab of cadmium-zinc-telluride with a density of 5.8 g/cm^3. Photon interactions in the detector panel were considered, including fluorescence. Energy deposited in each pixel was recorded and tallied in 1 keV bin widths. Therefore, the output of each simulation was an energy spectrum acquired in each detector pixel.

2.2.4. Conventional cone beam CT simulation

To compare the proposed imaging system with a more conventional CBCT system, the ^{155}Eu source spectrum was replaced by a typical 120 kV tungsten target X-ray tube spectrum. The geometry and detector material was left as in the ^{155}Eu simulation, however, all energy depositions were integrated so as to produce a single output value per pixel. Although conventional CBCT systems make use of aSi detector materials, the objective of this simulation was to highlight the differences in reconstructed images due to the use of the different source spectra.

2.3. Image reconstruction

The advantage of reconstructing DECT images for proton therapy dose calculation with an iterative algorithm known as total-variation superiorization with diagonally relaxed orthogonal projections (TVS-DROP) when compared to the traditional filtered backprojection (FBP) has been presented in previous work[20]. The TVS-DROP algorithm (referred to as TVS1-DROP* by Penfold *et al*.[21]) was once again used in the current work to reconstruct the 86.5 keV and 105.3 keV data. For details on the algorithmic implementation of TVS-DROP, the reader is referred to Zhu and Penfold[20].

Before starting the iterative reconstruction, data processing of the measured energy spectra from each pixel was required. A simulation of 10^{11} primary photons without the phantom in place was used to acquire an I_0 scan. To correct for panel Compton scattered 105.3 keV photons contributing to counts in the 86.5 keV channel, a linear fit to counts in the neighboring 3 energy bins larger than 86.5 keV were backprojected to the 86.5 keV bin. The backprojected counts were subtracted from the total 86.5 keV counts. To reduce noise in individual pixel energy spectra, the scatter correction was performed for each pixel by averaging the pixel spectra of the neighboring 3×3 pixels.

With the phantom at the centre of rotation of the imaging system, 180 simulations were performed with 10^{11} primary photons per projection angle with an angle spacing of 2 degrees. A consistent number of primary photons and projection angles were used in the 120 kV simulations. Air KERMA in air values of (9.9 ± 0.6) μGy and (9.6 ± 0.7) μGy in a 20 mm diameter sphere of air at isocenter were determined from Geant4 simulations for the ^{155}Eu and bremsstrahlung spectrum, respectively. The scatter correction processing as described above was performed for all projection angles for the Eu^{155} simulations.

2.4. SPR calculation by DECBCT images

The advantage of DECT imaging for proton therapy dose calculation has been investigated by several authors[7,8]. The advantage lies in the ability to calculate the SPR of tissues in a more direct manner than

with SECT. With DECT, the two attenuation coefficient images produced by image reconstruction may be processed to provide two separate images quantifying electron density and effective atomic number (Z_{eff})[22-24]. After converting Z_{eff} to mean excitation energy with the method proposed by Yang *et al.*[9], the SPR of a pixel can be calculated with Eq. (6).

$$SPR = \hat{\rho}_e \ln[\frac{2m_e c^2 \beta^2}{I_m(Z_{eff})\,(1-\beta^2)} - \beta^2] \,/\, \ln[\frac{2m_e c^2 \beta^2}{I_{water}(1-\beta^2)} - \beta^2] \quad (6)$$

here $\hat{\rho}_e$ is the electron density of the material relative to that of water, m_e is the rest electron mass, c is the speed of light in vacuum, β is the speed of the proton relative to the speed of light and $I_m(Z_{eff})$ and I_{water} are the mean excitation energies of the material and water respectively.

The Z_{eff} obtained by DECT was defined in the following manner. Let the attenuation coefficient of an element of atomic number Z at energy E be written as

$$\mu(E) = \rho_e \; {}_e\sigma(Z,E), \quad (7)$$

where ρ_e is the electron density and ${}_e\sigma$ is the total electronic cross-section. If we have two fixed photon energies and take the ratio of the attenuation coefficients, the energy independent electron density is cancelled and we are left with a function of atomic number only as shown in Eq. (8).

$$\frac{\mu_{E_1}}{\mu_{E_2}} = \frac{{}_e\sigma(Z,E_1)}{{}_e\sigma(Z,E_2)} = g(Z) \quad (8)$$

As the ratio of attenuation coefficients can be measured and the atomic number is unknown, we require the inverse of this function, i.e.

$$Z_{eff} = g^{-1}\left({}^{\mu_{E_1}}/_{\mu_{E_2}}\right) = f({}^{\mu_{86.5}}/_{\mu_{105.3}}) \quad (9)$$

Attenuation coefficients for 86.5 keV and 105.3 keV were obtained from NIST XCOM for atomic numbers 6 – 15. Z was plotted as a function of the resulting ratio. A fourth degree polynomial function was fit to

this data to provide the function *f* of Eq. (9) (see Fig. 3.). This function was applied to the ratio of each reconstructed pixel value of the DECBCT simulations.

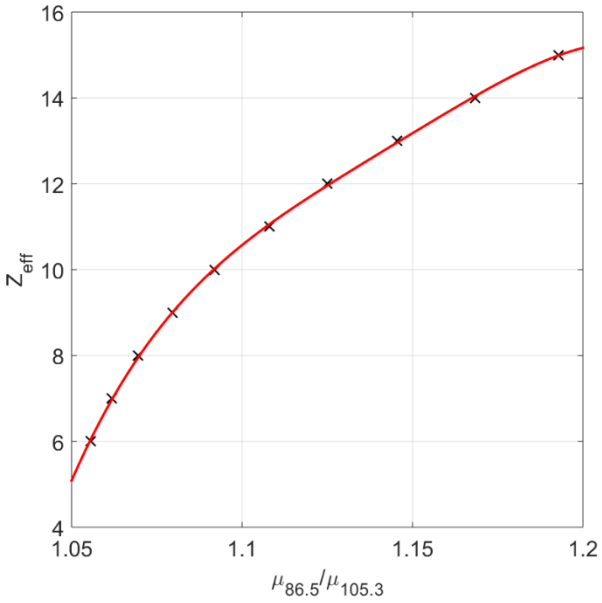

Figure 3. Relationship between atomic number and ratio of attenuation coefficients at 86.5 keV and 105.3 keV. NIST XCOM data points are shown in black and the fourth degree polynomial fit to the data shown in red.

A stoichiometric calibration of the natural logarithm of mean excitation energy as a function of Z_{eff} was performed as described in Yang *et al.*[9] and Zhu and Penfold[11]. In this process, the chemical composition and density of ICRU 44 tissues were used to calculate mean excitation energies with Eq. (10) and Z_{eff} with Eq. (9).

$$\ln I_m = \frac{\sum \frac{\omega_i Z_i}{A_i} \times \ln I_i}{\sum \frac{\omega_i Z_i}{A_i}} \tag{10}$$

Here ω_i is the weight of element *i* in a given tissue, *Z* is the atomic number and *A* is atomic weight. I_i represents the mean excitation energy of element *i*. The relationship between Z_{eff} and ln I_m was approximated with a piecewise linear fit to the data, as described in Zhu and Penfold[11].

2.5. Analysis of SPR

2.5.1. Reference SPR calculation

To compare the accuracy of SPR calculated by DECBCT with that derived from CBCT, a reference SPR image was required. This image was obtained by applying Eq. (6) to all pixels with the chemical compositions and densities of tissues presented in Table 2. Here, the electron density was calculated with Eq. (11)[25].

$$\rho_e = \rho N_g / \rho^w N_g^w \tag{11}$$

Where ρ is the density of tissue, N_g is the number of electrons per unit volume in the tissue, ρ^w is the density of water, and N_g^w denotes the number of electrons per unit volume in water.

The mean excitation energy, I, of the tissues was calculated with Eq. (10) and the proton kinetic energy set to 219 MeV, as in Yang *et al.*[9].

2.5.2. SPR with polyenergetic spectrum and TVS-DROP algorithm

Schneider *et al*.[25] suggested the use of a stoichiometric calibration to transfer X-ray CT images to SPR values for proton therapy dose calculation. This process was applied for the 120 kV spectra and ICRU 44 tissues used in the current work. It is equivalent to the calibration of ln I_m as a function of Z_{eff} described above, however, SPR replaces ln I_m and the attenuation coefficient replaces Z_{eff}. SPR was calculated with Eq. (6) using the method outlined in Section 2.5.1 but with ICRU 44 tissues instead of the phantom tissues. The attenuation coefficients for ICRU 44 tissues with the 120 kV spectra were obtained from NIST XCOM[26]. Fig. 4 illustrates the stoichiometric calibrations for DECT and SECT.

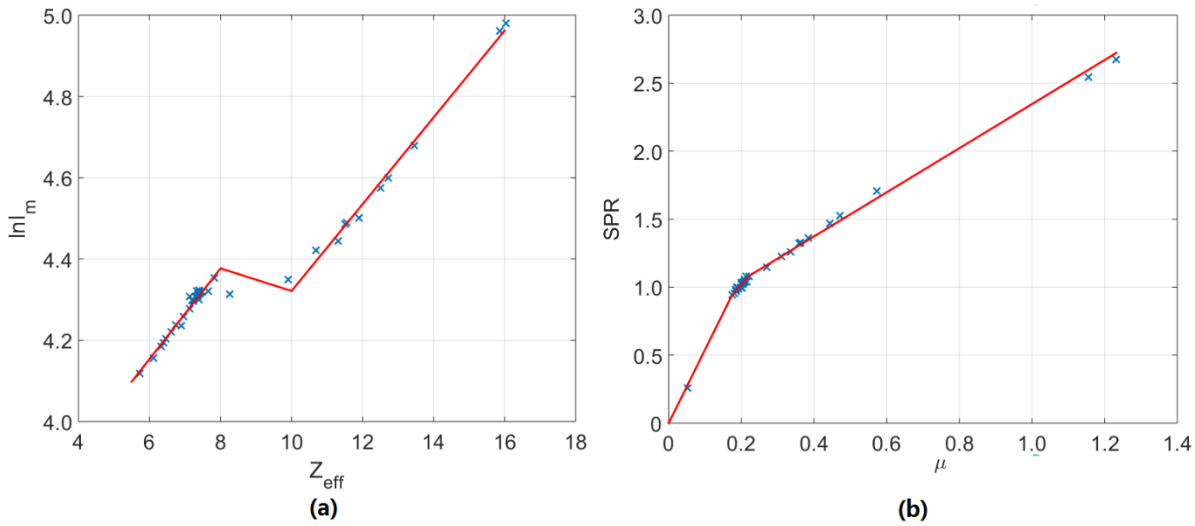

Figure 4. Stoichiometric calibration functions for (a) DECT and (b) SECT. Crosses correspond to data points calculated for ICRU 44 tissues, lines represent a piecewise linear fit to the data.

3. Results

3.1. Acquired energy spectra

An example of the energy spectrum collected by a single pixel, located in the central region of the panel, is shown in Fig. 5. In addition to the original 86.5 keV and 105.3 keV peaks, several other peaks are now present. The origin of these peaks are summarized in Table 4. The peaks are caused by characteristic X-rays originating in the pixel of photoelectric interaction being detected in a neighboring pixel. As a result, a peak is seen in energy bins corresponding to the energy of the characteristic X-ray, and also the energy bin corresponding to the difference between the original photon energy and the characteristic X-ray energy. In the future these peaks may be included in the counts for the respective photon peaks, but due to the difficulty with subtracting the scatter background from these energy bins, they were not utilized in the current work.

As discussed in Section 2.3, a small contribution from Compton scattered 105.3 keV photons can be seen to contribute to counts in the 86.5 keV peak. By comparing the relative height of the peak to the

background from acquisitions with and without the phantom, it was determined that the majority of the Compton scattered photons originate from interactions in the panel, rather than interactions in the phantom.

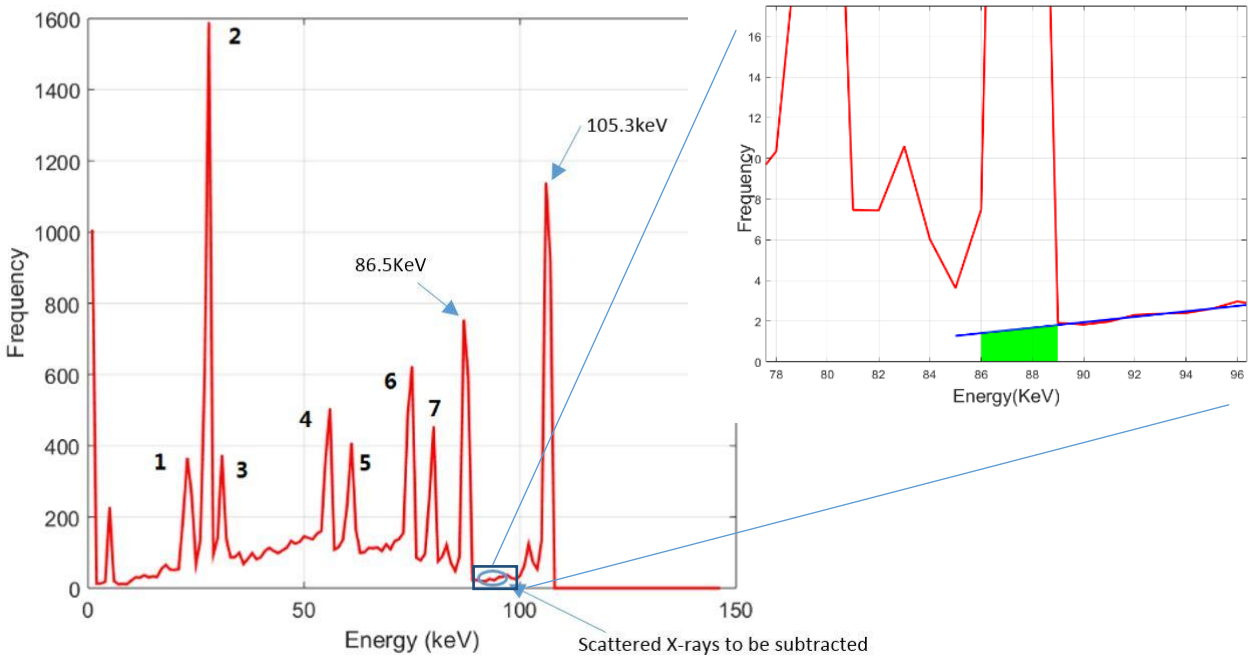

Figure 5. Example energy spectra acquired in a single pixel of the CZT detector. The insert contains a zoomed image illustrating how 105.5 keV scattered X-rays were subtracted from the 86.5 keV photopeak. The blue line is a straight line fit to the three bins immediately larger than the 86.5 keV bin and the green region is the subtracted scattered photon contribution.

Table 4. Origin of dominant peaks appearing in detected spectra not present in source spectrum.

ID	Energy bin (keV)	Origin
1	23	Cd K_α (23.2 keV)
2	27	Te K_α (27.5 keV)
3	31	Te K_β (31.0 keV)
4	55	86.5 keV - Te K_β
5	60	86.5 keV - Te K_α
6	73	105.3 keV - Te K_β
7	78	105.3 keV - Te K_α

3.2. Reconstructed CBCT images

Attenuation coefficient images for the 86.5 keV and 105.3 keV peaks reconstructed with TVS-DROP are shown in Fig. 6 (a) and (b). Also shown are images reconstructed with TVS-DROP using data acquired with the 120 kV source spectrum in Fig. 6 (c). As the attenuation coefficients are different for each image, custom window settings were used. The lower window level was set to half the reference value for brain tissue, and the upper level set to 1.1 times the expected value for the bone. This choice of window level setting resulted in a generally darker display for the image corresponding to the 120 kV source spectrum with TVS-DROP reconstruction (Fig. 6(c)). This can be explained by the relatively larger attenuation coefficient of cranium with respect to brain for the 120 kV spectrum, making the upper window boundary higher.

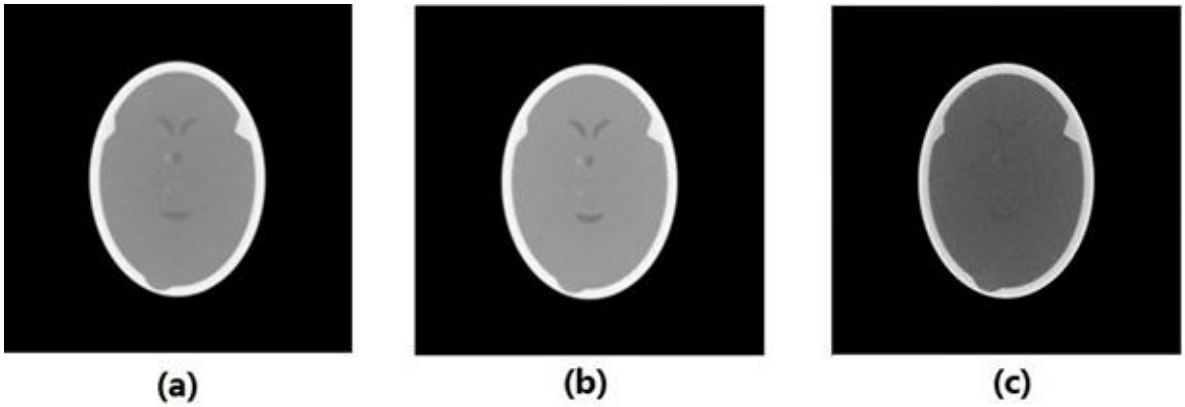

Figure 6. A slice of the 3D reconstructed images for (a) 86.5 keV, (b) 105.3 keV, (c) 120 kV spectrum reconstructed with the TVS-DROP algorithm.

Table 5. Summary of reconstructed pixel values for the cranium and brain regions of the images shown in Fig. 4. Simulated values correspond to mean pixel values ± 1 standard deviation over a region of interest. Reference values at 120 kV were calculated with 10 cm water filtration applied to the incident spectrum to account for beam hardening in the phantom.

		86.5 keV with TVS-DROP	105.3 keV with TVS-DROP	120 kV with TVS-DROP
Cranium	Simulated	0.315 ± 0.008	0.279 ± 0.005	0.475 ± 0.034
	Reference	0.320	0.280	0.482
	% diff.	*-1.56%*	*-0.36%*	*-1.47%*
Brain	Simulated	0.181 ± 0.003	0.175 ± 0.002	0.212 ± 0.007
	Reference	0.184	0.173	0.210
	% diff.	*-1.63%*	*1.16%*	*-0.95%*

The noise reduction and associated superiority in contrast resolution when using monoenergetic imaging is evident. A summary of the reconstructed values for the cranium and brain regions of the images shown in Fig. 6 is presented in Table 5. All measured values agree with reference values within one standard deviation. The greatest difference can be seen in the standard deviation values, indicating differing degrees of noise in the images.

3.3. SPR accuracy with DECBCT and CBCT approaches

Images obtained following conversion of the DECBCT and 120 kV CBCT images to SPR are shown in Fig. 7 and compared to the reference image. Since the conversion of the 120 kV images is obtained by a simple mapping with a linear function, the images do not appear different to those shown in Fig. 6. However, the conversion of the DECBCT images to SPR requires a ratio of the two images and as such the noise in the resulting image is amplified when compared to the two original images. Even so, superior contrast resolution is still evident when using the ^{155}Eu spectrum.

Figure 7. (a) Reference SPR image. Reconstructed SPR images using (b) the DECBCT approach, (c) using the 120 kV CBCT image reconstructed with TVS-DROP. All images are displayed with an equivalent SPR window setting.

To compare the quantitative accuracy of the SPR images, a histogram of pixel values was generated for each reconstructed image, as well as the reference SPR image. The histogram is shown in Fig. 8. The pixelwise relative difference with respect to the reference phantom was also calculated and the frequency historgram of the error maps are shown in Fig. 9. Comparing the location of peak values and width of the peaks of Fig. 8 demonstrates the superior accuracy and precision, respectively, of the ^{155}Eu DECBCT SPR image. This is further supported by the relative error plots shown in Fig. 9. A comparison of the cranium and brain values for the three reconstructed images is provided in Table 6. SPR accuracy

within 1% was obtained when using ^{155}Eu DECBCT. The accuracy was reduced for the conventional CBCT approach.

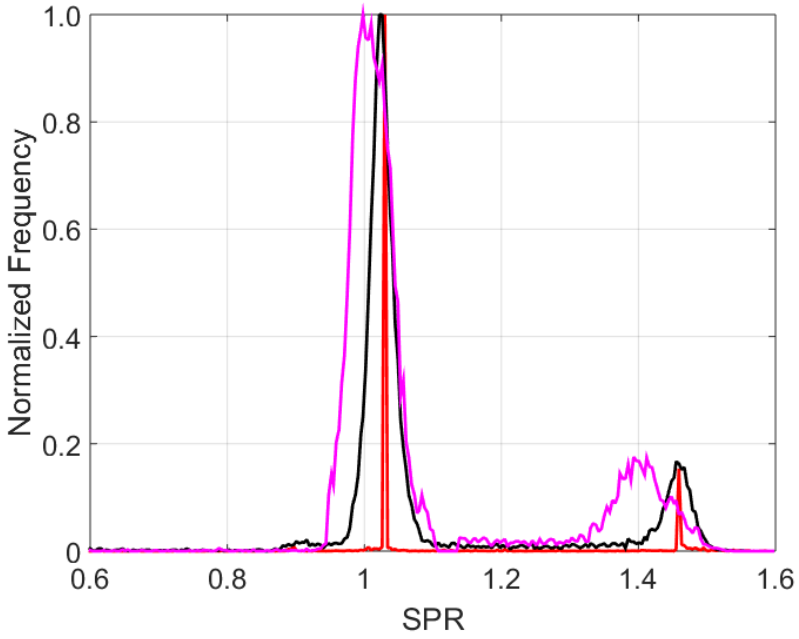

Figure 8. Histogram of SPR images. Reference (red), ^{155}Eu DECBCT (black), and 120 kV X-ray spectrum (pink).

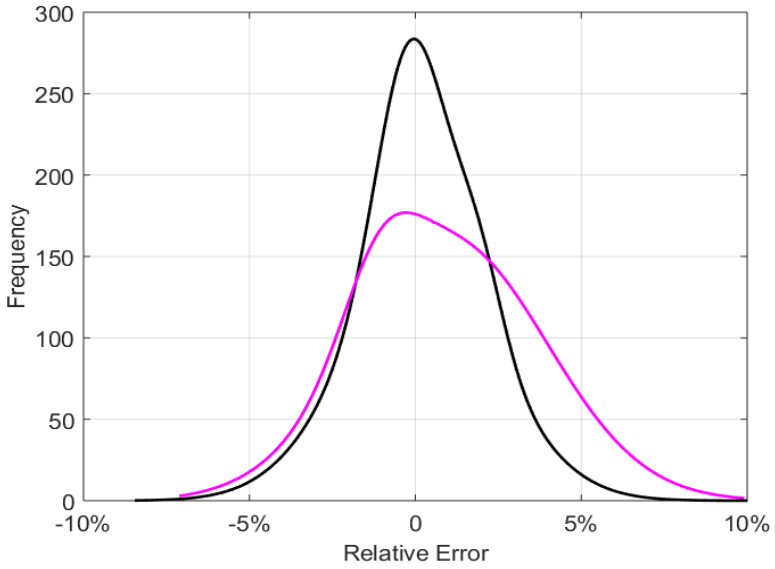

Figure 9. Frequency histogram of pixel-wise relative errors in the reconstructed images shown in Fig. 7. ^{155}Eu DECBCT (black), and 120 kV X-ray spectrum (pink).

Table 6. Comparison of SPR derived from images generated with ^{155}Eu DECBCT and 120 kV SECT.

Tissue	Reference SPR	^{155}Eu DECBCT	% diff.	120 kV SECT	% diff.
Cranium	1.463	1.455 ± 0.024	-0.55%	1.406 ± 0.042	-3.90%
Brain	1.031	1.022 ± 0.017	-0.87%	1.013 ± 0.020	-1.75%

4. Discussion

As schemes for online adaptive radiotherapy continue to evolve, the need for quantitatively accurate 3D imaging immediately prior to treatment increases. This is particularly true for proton therapy due to the sensitivity of Bragg peak positioning upon estimated tissue SPR. For this purpose, a DECBCT imaging system based on ^{155}Eu and a CZT detector panel has been proposed in the current work. The potential advantages in terms of SPR accuracy for online adaptive proton therapy dose calculation have been presented.

Calculations showed that a source diameter of approximately 5 mm would be required to allow imaging with 1 revolution per minute while ensuring sufficient counts per pixel for 2% Poisson counting uncertainty for a 1 mm^2 pixel size. Reconstructed images did not show significant degradation of spatial resolution with this large source size, however further work is required to quantify the effect this may have on dose calculation accuracy for adaptive radiotherapy. By modifying the parameters discussed in Section 2.1 it was found that doubling the pixel size reduced the required source diameter by 30% while allowing for 5% counting uncertainty allowed for a reduction of source diameter of approximately 50%. Increasing the acquisition time has the smallest effect on required source size. The calculations also assumed 100% purity of the ^{155}Eu source. The fraction of ^{155}Eu nuclei in the source will be less than 1 in reality and decrease over time. It is envisaged that source decay would be accounted for in the rotation speed of the imaging system.

Quantitatively accurate reconstructions of attenuation coefficients for both gamma emissions were presented. Superior contrast resolution due the absence of beam hardening and Compton scatter removal was demonstrated when compared to images generated with conventional 120 kV bremsstrahlung spectra. A method for conversion of the monoenergetic attenuation coefficient images to SPR was presented. Reconstructed SPR values were within 1% of the reference values calculated from the known chemical composition and density of the materials used in the Geant4 simulation. This was compared to an error of 3.9% for cranium SPR when using a 120 kV source spectrum. A quantitative comparison of spatial resolution and contrast resolution will be conducted in future work with appropriate phantoms.

A head phantom was used to demonstrate the concept in the current work. Further work is required to demonstrate the functionality of the proposed imaging concept with larger treatment sites such as the abdomen and thorax. These sites typically make use of bow-tie filters to reduce the range of X-ray fluence at the detector panel. Furthermore, conventional X-ray tubes allow for an increase in mAs to

compensate for the extra attenuation experienced when traversing the body. The only corresponding control mechanism in the proposed ^{155}Eu imaging system is a longer acquisition time. This may be achieved by a variable rotation speed, accounting for variable patient thicknesses.

The limited count-rate of ^{155}Eu imaging is advantageous, however, when considering the need to avoid count pile-up in the solid state detector panel. While the critical time to avoid pile-up in the detector is heavily dependent on design and construction, one can expect to avoid significant pile-up contribution with count rates of 1 MHz or less[27]. Indeed, one manufacturer quotes pixelated detector capabilities of 10^7 photons/s/pixel. For the proposed imaging concept, it is envisaged that maximum count rates on the order of $10^4 – 10^5$ photons/s/pixel would be experienced outside the imaged object. Pile-up is therefore not thought to be a limiting factor.

The detector simulated in the current work was 10 mm thick, which is larger than pixelated systems currently available on the market. Due to the large atomic number and thus high photoelectric cross-section, reducing the thickness to 2 mm reduces the photoelectric absorption in the detector by only 0.3% at 105.3 keV. Further simulation and experimental work is required to optimize the system design, however, it is not anticipated that detector thickness will significantly affect the detection efficiency at 105.3 keV. An additional detector-related aspect that warrants examination in an experimental system is energy response. In a first approximation electronic noise and charge sharing amongst neighboring pixels was neglected in the current work. Schlomka *et al.*[28] have shown that charge sharing in particular can lead to a significant degradation in the energy resolution of CdTe pixelated detectors if not accounted for.

Advances in conventional CBCT are still taking place and need to be considered in future comparisons with ^{155}Eu-based imaging. In particular, dual energy CBCT systems and detectors with antiscatter grids are currently being investigated. Dual energy cone beam CT with conventional flat panel detectors and

X-ray tubes have been explored for image guided radiotherapy[29]. These systems are in a prototype stage and as such comparisons with our approach are not yet feasible. CBCT systems with antiscatter grids have been investigated by Schafer *et. al*[30]. It was determined that although the antiscatter grid could improve HU accuracy, CNR was compromised and thus the authors did support the use of antiscatter grids for CBCT.

5. Conclusion

A novel dual energy cone beam CT system consisting of a ^{155}Eu source and a pixelated CZT detector panel for applications in adaptive proton therapy has been presented. A realistic source size was used for Monte Carlo CT simulations of a head phantom. A method to convert the reconstructed monoenergetic emissions of ^{155}Eu to SPR was presented. Images generated with the ^{155}Eu-CZT system were found to contain less noise than those reconstructed with a typical 120 kV bremsstrahlung source spectrum. The proposed imaging modality may provide a new alternative for 3D imaging for adaptive radiotherapy and proton therapy in particular.

References

1. Yan D, Vicini F, Wong J, Martinez A. Adaptive radiation therapy. *Physics in medicine and biology.* 1997;42(1):123.
2. Foroudi F, Wong J, Haworth A, et al. Offline adaptive radiotherapy for bladder cancer using cone beam computed tomography. *Journal of medical imaging and radiation oncology.* 2009;53(2):226-233.
3. Veiga C, Alshaikhi J, Amos R, et al. Cone-beam computed tomography and deformable registration-based "dose of the day" calculations for adaptive proton therapy. *International Journal of Particle Therapy.* 2015;2(2):404-414.
4. Kurz C, Nijhuis R, Reiner M, et al. Feasibility of automated proton therapy plan adaptation for head and neck tumors using cone beam CT images. *Radiation Oncology.* 2016;11(1):64.
5. Landry G, Nijhuis R, Dedes G, et al. Investigating CT to CBCT image registration for head and neck proton therapy as a tool for daily dose recalculation. *Medical physics.* 2015;42(3):1354-1366.
6. Kurz C, Dedes G, Resch A, et al. Comparing cone-beam CT intensity correction methods for dose recalculation in adaptive intensity-modulated photon and proton therapy for head and neck cancer. *Acta Oncologica.* 2015;54(9):1651-1657.
7. Guan H, Dong H. Dose calculation accuracy using cone-beam CT (CBCT) for pelvic adaptive radiotherapy. *Physics in medicine and biology.* 2009;54(20):6239.

8. Hatton J, McCurdy B, Greer PB. Cone beam computerized tomography: the effect of calibration of the Hounsfield unit number to electron density on dose calculation accuracy for adaptive radiation therapy. *Physics in medicine and biology.* 2009;54(15):N329.
9. Yang M, Virshup G, Clayton J, Zhu X, Mohan R, Dong L. Theoretical variance analysis of single- and dual-energy computed tomography methods for calculating proton stopping power ratios of biological tissues. *Physics in medicine and biology.* 2010;55(5):1343.
10. Hudobivnik N, Schwarz F, Johnson T, et al. Comparison of proton therapy treatment planning for head tumors with a pencil beam algorithm on dual and single energy CT images. *Medical physics.* 2016;43(1):495-504.
11. Zhu J, Penfold SN. Dosimetric comparison of stopping power calibration with dual-energy CT and single-energy CT in proton therapy treatment planning. *Medical Physics.* 2016;43(6):2845-2854.
12. Stewart PJ. Method for Radiography. *US Patent Office.* (1954;US2675368.
13. F.N.Case EHA, N.H.Cutshall. Production Study of Gadolinium-153. *Isotopes Division.* 1969;Oakridge National Laboratory.
14. Nuclear Data Center at KAERI. Table of γ -rays. *[online].*Available at : http://atom.kaeri.re.kr/.
15. Agostinelli S. Geant4 collaboration. *Nucl Instrum Methods A.* 2003;506(250):01368-01368.
16. D.E. Cullen JHH, L.Kissel. EPDL97: The Evaluated Photon Data Library '97 Version. *UCRL.* 1997;6 Rev.5.
17. Herman GT, Davidi R. Image reconstruction from a small number of projections. *Inverse problems.* 2008;24(4):045011.
18. Richmond C. ICRP publication 23. *International Journal of Radiation Biology and Related Studies in Physics, Chemistry and Medicine.* 1985;48(2):285-285.
19. Le HQ, Ducote JL, Molloi S. Radiation dose reduction using a CdZnTe-based computed tomography system: Comparison to flat-panel detectors. *Medical physics.* 2010;37(3):1225-1236.
20. Zhu J, Penfold SN. Total Variation Superiorization in Dual-energy CT Reconstruction for Proton Therapy Treatment Planning. *Inverse Problems submitted.* (2016.
21. Penfold S, Schulte RW, Censor Y, Rosenfeld AB. Total variation superiorization schemes in proton computed tomography image reconstruction. *Medical physics.* 2010;37(11):5887-5895.
22. Bazalova M, Carrier J-F, Beaulieu L, Verhaegen F. Dual-energy CT-based material extraction for tissue segmentation in Monte Carlo dose calculations. *Physics in medicine and biology.* 2008;53(9):2439.
23. Torikoshi M, Tsunoo T, Sasaki M, et al. Electron density measurement with dual-energy x-ray CT using synchrotron radiation. *Physics in medicine and biology.* 2003;48(5):673.
24. Landry G, Parodi K, Wildberger JE, Verhaegen F. Deriving concentrations of oxygen and carbon in human tissues using single-and dual-energy CT for ion therapy applications. *Physics in medicine and biology.* 2013;58(15):5029.
25. Schneider U, Pedroni E, Lomax A. The calibration of CT Hounsfield units for radiotherapy treatment planning. *Physics in medicine and biology.* 1996;41(1):111.
26. Berger MJ, Hubbell J, Seltzer S, et al. XCOM: photon cross sections database. *NIST Standard reference database.* 1998;8:87-3597.
27. Feuerlein S, Roessl E, Proksa R, et al. Multienergy Photon-counting K-edge Imaging: Potential for Improved Luminal Depiction in Vascular Imaging. *Radiology.* 2008;249(3):1010-1016.
28. Schlomka JP, Roessl E, Dorscheid R, et al. Experimental feasibility of multi-energy photon-counting K-edge imaging in pre-clinical computed tomography. *Physics in medicine and biology.* 2008;53(5):16.
29. H Li WG, J Bowsher, FF Yin. A dual cone-beam CT system for image guided radiotherapy: initial performance characterization. *Medical physics.* 2013;40(2).

30. Schafer S, W. Stayman J, Zbijewski W, Schmidgunst C, Kleinszig G, H. Siewerdsen J. Antiscatter grids in mobile C-arm cone-beam CT: Effect on image quality and dose. *Medical Physics.* 2012;39(1):153-159.